

On the Spurious Interior Resonance Modes of Time Domain Integral Equations for Analyzing Acoustic Scattering from Penetrable Objects

Rui Chen¹, Yifei Shi², Sadeed Bin Sayed³, Mingyu Lu⁴, and Hakan Bagci¹

¹*Division of Computer, Electrical, and Mathematical Science and Engineering, King Abdullah University of Science and Technology, Thuwal 23955-6900, Saudi Arabia
rui.chen@kaust.edu.sa*

²*Department of Electronic Engineering, Jiangsu University of Technology, Changzhou, Jiangsu 213001, China*

³*Halliburton Far East Pte. Ltd., 639940, Singapore*

⁴*Department of Electrical and Computer Engineering, West Virginia University Institute of Technology, Beckley, WV 25801, United States*

Abstract

The interior resonance problem of time domain integral equations (TDIEs) formulated to analyze acoustic field interactions on penetrable objects is investigated. Two types of TDIEs are considered: The first equation, which is termed the time domain potential integral equation (TDPIE) (in unknowns velocity potential and its normal derivative), suffers from the interior resonance problem, i.e., its solution is replete with spurious modes that are excited at the resonance frequencies of the acoustic cavity in the shape of the scatterer. Numerical experiments demonstrate that, unlike the frequency-domain integral equations, the amplitude of these modes in the time domain could be suppressed to a level that does not significantly affect the solution. The second equation is obtained by linearly combining TDPIE with its normal derivative. Weights of the combination are carefully selected to enable the numerical computation of the singular integrals. The solution of this equation, which is termed the time domain combined potential integral equation (TDCPIE), does not involve any spurious interior resonance modes.

Keywords: *Acoustic scattering, Acoustic transmission, Penetrable scatterer, Time domain integral equation, Spurious interior resonance problem, Numerical error*

1 Introduction

Many applications in engineering and physical sciences call for simulations of acoustic scattering from penetrable objects, i.e., scatterers that internally support nonzero velocity potential and pressure field [1–10]. An acoustic scattering problem involving penetrable objects is also known as an acoustic transmission problem. The time-harmonic (frequency-domain) acoustic transmission problem can be analyzed by solving a set of integral equations enforced on the surface of the scatterer [11]. This set of equations is obtained by using the Kirchhoff-Helmholtz theorem to express the scattered fields of the exterior and interior problems in terms of (unknown) velocity potential on the surface of the scatterer and its normal derivative. The exterior and interior problems involve the unbounded domains with the material properties (density and wave speed) of the background medium and the scatterer, respectively. Numerical schemes developed to solve these integral equations discretize only the surface of the scatterer and implicitly enforce the radiation condition at infinity [11], offering advantages over finite element and finite difference methods that directly solve the Helmholtz equation, and require a volumetric discretization of the whole computation domain and use absorbing boundary conditions on its surface to approximate the radiation condition.

On the other hand, traditional integral equation formulations suffer from so-called “interior resonance” problem [12–20]. This problem is observed when the excitation frequency approaches any one of the resonance frequencies of the acoustic cavity in the shape of the scatterer and has the density and the wave speed of the background medium. At these frequencies the surface integral operator has a null space and the corresponding equation does not have a unique solution. Several approaches have been proposed to address the interior resonance problem of the frequency-domain integral equations. Examples of these include the combined Helmholtz integral equation formulation [12] and the Burton-Miller scheme [13].

Even though interior resonance problem is well-studied for the frequency-domain integral equations, there are only a couple of studies that investigate the spurious interior resonance modes in the solution of time domain integral equations (TDIEs) of acoustics [21–24]. In [21], a spurious resonance-free Burton-Miller-type time domain combined field integral equation is formulated to

analyze acoustic scattering from sound-rigid bodies. In [25], interior resonance modes observed in the solution of the time domain electric field integral equation (of electromagnetics) that is enforced on perfect electrically conducting scatterers are investigated. Theoretically, TDIEs should not admit any interior resonance modes since their solution is obtained under zero initial condition and the interior resonance modes do not satisfy this initial condition [25, 26]. But the interior resonance modes are still observed in the time domain solutions. It is discussed in [25] that this is because of the numerical errors introduced due to discretization and matrix inversions carried out during time marching.

In this work, the interior resonance problem of two different TDIEs formulated to analyze the transient acoustic transmission problem is investigated: The first equation, which is termed time domain potential integral equation (TDPIE) (in unknowns velocity potential and its normal derivative) here, is the time-domain equivalent of the frequency-domain integral equation that is traditionally used in the literature to solve the acoustic transmission problem [5, 8, 9, 27]. This equation suffers from the interior resonance problem. Its solution is replete with spurious modes that oscillate (without any decay) with the resonance frequencies of the acoustic cavity in the shape of the scatterer and has the density and the wave speed of the background medium [14]. These modes are excited when their resonance frequency is within the band of the excitation. In this work, it is demonstrated that unlike the frequency-domain integral equations, the amplitude of these modes in the time domain could be suppressed to a level, which does not significantly affect the solution, by increasing the accuracy of the discretization. This is achieved by using band-limited temporal basis functions and using smaller time step sizes. On the other hand, the second equation investigated in this work, which is termed time domain combined potential integral equation (TDCPIE), completely eliminates the interior resonance problem. The frequency-domain counterpart of TDCPIE has been introduced in [7] and it has been theoretically shown that its frequency-domain solution is unique at the interior resonance frequencies. Numerical results in this work verify that TDCPIE does not admit any interior resonance modes. It should be noted here that TDCPIE is obtained by linearly combining TDPIE with its normal derivative. Coupling parameters of this combination are carefully selected to enable the computation of the singular integrals that

appear in the expressions of the matrix elements resulting from the Nyström discretization in space [28–40].

The remainder of this paper is organized as follows. In Section 2, TDPIE and TDCPIE are derived. Section 3 describes the spatial and temporal discretization schemes and the marching-on-in-time method that is used to solve the resulting matrix system. In Section 4, numerical results are presented to validate the accuracy of TDPIE and TDCPIE solutions and demonstrate the relationship between the numerical errors and the interior resonance modes observed in the solution of the TDPIE. Section 5 concludes the paper with a short summary.

2 Formulation

Let Ω_2 denote the support of an acoustically penetrable scatterer, which resides in an unbounded homogeneous background medium that is denoted by Ω_1 (Fig. 1). Let S represent the surface that separates these two domains, i.e., the surface of the scatterer. The wave speed and the density in Ω_k , $k \in \{1, 2\}$, are c_k and ρ_k , respectively. An acoustic field with velocity potential $\varphi^i(\mathbf{r}, t)$ is incident on S . It is assumed that $\varphi^i(\mathbf{r}, t)$ is band-limited to maximum frequency f_{\max} and vanishingly small for $t \leq 0$ on $\mathbf{r} \in S$. In response to this excitation, scattered fields with velocity potentials $\varphi_k^s(\mathbf{r}, t)$ are generated in Ω_k . Total velocity potentials in Ω_1 and Ω_2 are expressed as $\varphi_1(\mathbf{r}, t) = \varphi^i(\mathbf{r}, t) + \varphi_1^s(\mathbf{r}, t)$ and $\varphi_2(\mathbf{r}, t) = \varphi_2^s(\mathbf{r}, t)$, respectively.

Using the Kirchhoff-Helmholtz theorem [41], $\partial_t \varphi_1(\mathbf{r}, t)$ and $\partial_t \varphi_2(\mathbf{r}, t)$ are expressed as [27]

$$\partial_t \varphi_1(\mathbf{r}, t) = \partial_t \varphi^i(\mathbf{r}, t) - \partial_t S_1[\partial_n \varphi_1](\mathbf{r}, t) + \partial_t D_1[\varphi_1](\mathbf{r}, t), \mathbf{r} \in \Omega_1, \quad (1)$$

$$\partial_t \varphi_2(\mathbf{r}, t) = \partial_t S_2[\partial_n \varphi_2](\mathbf{r}, t) - \partial_t D_2[\varphi_2](\mathbf{r}, t), \mathbf{r} \in \Omega_2. \quad (2)$$

Here, ∂_t denotes the temporal derivative, $\partial_n = \hat{\mathbf{n}}(\mathbf{r}) \cdot \nabla$, $\hat{\mathbf{n}}(\mathbf{r})$ is the outward pointing unit normal

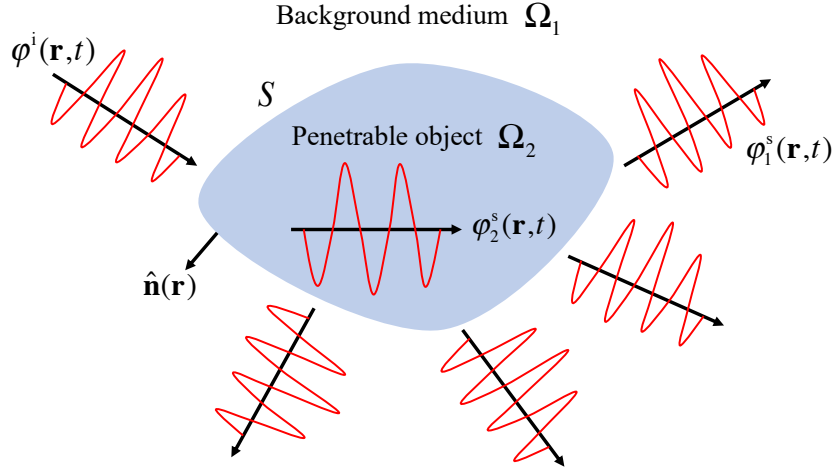


Figure 1: Description of the acoustic scattering problem.

at point $\mathbf{r} \in S$, and the spatio-temporal integral operators $S_k[x](\mathbf{r}, t)$ and $D_k[x](\mathbf{r}, t)$ are given by

$$S_k[x](\mathbf{r}, t) = \int_S G_k(|\mathbf{r} - \mathbf{r}'|, t) * x(\mathbf{r}', t) ds',$$

$$D_k[x](\mathbf{r}, t) = \int_S \partial_{n'} G_k(|\mathbf{r} - \mathbf{r}'|, t) * x(\mathbf{r}', t) ds',$$

where “*” denotes temporal convolution and

$$G_k(|\mathbf{r} - \mathbf{r}'|, t) = \frac{\delta(t - |\mathbf{r} - \mathbf{r}'|/c_k)}{4\pi |\mathbf{r} - \mathbf{r}'|}$$

is the time domain Green function. Note that since the Green function is in the form of a Dirac delta function $\delta(t - t_0)$, the temporal convolutions in operators $S_k[x](\mathbf{r}, t)$ and $D_k[x](\mathbf{r}, t)$ reduce retarded time integrals.

On S , the acoustic pressure field and the normal component of the velocity field are continuous, i.e., the velocity potential satisfies the following boundary conditions [27]:

$$\rho_1 \partial_t \varphi_1(\mathbf{r}, t) = \rho_2 \partial_t \varphi_2(\mathbf{r}, t), \mathbf{r} \in S, \quad (3)$$

$$\partial_n \varphi_1(\mathbf{r}, t) = \partial_n \varphi_2(\mathbf{r}, t), \mathbf{r} \in S. \quad (4)$$

2.1 TDPIE

Taking the limit of Eqs. (1) and (2) as \mathbf{r} approaches S from Ω_k , $k \in \{1, 2\}$ and inserting Eqs. (3) and (4) into the resulting equations yield TDPIE as [27]

$$\frac{1}{2}\partial_t\varphi_1(\mathbf{r}, t) = \partial_t\varphi^i(\mathbf{r}, t) - \partial_t S_1[\partial_n\varphi_1](\mathbf{r}, t) + \partial_t\tilde{D}_1[\varphi_1](\mathbf{r}, t), \mathbf{r} \in S, \quad (5)$$

$$\frac{\rho_1}{2\rho_2}\partial_t\varphi_1(\mathbf{r}, t) = \partial_t S_2[\partial_n\varphi_1](\mathbf{r}, t) - \frac{\rho_1}{\rho_2}\partial_t\tilde{D}_2[\varphi_1](\mathbf{r}, t), \mathbf{r} \in S. \quad (6)$$

Here, “ \sim ” on top of \tilde{D}_k means that the space integral in D_k is evaluated in the principal value sense [42].

2.2 TDCPIE

Taking the normal derivative of Eqs. (1) and (2) yields

$$\partial_t\partial_n\varphi_1(\mathbf{r}, t) = \partial_t\partial_n\varphi^i(\mathbf{r}, t) - \partial_t D'_1[\partial_n\varphi_1](\mathbf{r}, t) + \partial_t N_1[\varphi_1](\mathbf{r}, t), \mathbf{r} \in \Omega_1, \quad (7)$$

$$\partial_t\partial_n\varphi_2(\mathbf{r}, t) = \partial_t D'_2[\partial_n\varphi_2](\mathbf{r}, t) - \partial_t N_2[\varphi_2](\mathbf{r}, t), \mathbf{r} \in \Omega_2, \quad (8)$$

where the spatio-temporal integral operators $D'_k[x](\mathbf{r}, t)$ and $N_k[x](\mathbf{r}, t)$ are given by

$$D'_k[x](\mathbf{r}, t) = \int_S \partial_n G_k(|\mathbf{r} - \mathbf{r}'|, t) * x(\mathbf{r}', t) ds',$$

$$N_k[x](\mathbf{r}, t) = \int_S \partial_{nn'}^2 G_k(|\mathbf{r} - \mathbf{r}'|, t) * x(\mathbf{r}', t) ds',$$

and $\partial_{nn'}^2 = \partial_n\partial_{n'}$ denotes the double normal derivative. Taking the limit of Eqs. (7) and (8) as \mathbf{r} approaches S from Ω_k , $k \in \{1, 2\}$ and inserting Eqs. (3) and (4) into the resulting equations yield the normal derivative of TDPIE in Eqs. (5) and (6) as

$$\frac{1}{2}\partial_t\partial_n\varphi_1(\mathbf{r}, t) = \partial_t\partial_n\varphi^i(\mathbf{r}, t) - \partial_t\tilde{D}'_1[\partial_n\varphi_1](\mathbf{r}, t) + \partial_t N_1[\varphi_1](\mathbf{r}, t), \mathbf{r} \in S, \quad (9)$$

$$\frac{1}{2}\partial_t\partial_n\varphi_1(\mathbf{r}, t) = \partial_t\tilde{D}'_2[\partial_n\varphi_1](\mathbf{r}, t) - \frac{\rho_1}{\rho_2}\partial_t N_2[\varphi_1](\mathbf{r}, t), \mathbf{r} \in S. \quad (10)$$

Linearly combining Eqs. (5)-(6) and (9)-(10) as $\alpha_1(5)+\alpha_2\frac{\rho_2}{\rho_1}(6)$ and $\beta_1(9)+\beta_2(10)$ yields TDCPIE as

$$\begin{aligned} & \frac{\alpha_1 + \alpha_2}{2} \partial_t \varphi_1(\mathbf{r}, t) - \alpha_1 \partial_t \tilde{D}_1[\varphi_1](\mathbf{r}, t) + \alpha_2 \partial_t \tilde{D}_2[\varphi_1](\mathbf{r}, t) \\ & + \alpha_1 \partial_t S_1[\partial_n \varphi_1](\mathbf{r}, t) - \alpha_2 \frac{\rho_2}{\rho_1} \partial_t S_2[\partial_n \varphi_1](\mathbf{r}, t) = \alpha_1 \partial_t \varphi^i(\mathbf{r}, t), \mathbf{r} \in S, \end{aligned} \quad (11)$$

$$\begin{aligned} & - \beta_1 \partial_t N_1[\varphi_1](\mathbf{r}, t) + \beta_2 \frac{\rho_1}{\rho_2} \partial_t N_2[\varphi_1](\mathbf{r}, t) + \frac{\beta_1 + \beta_2}{2} \partial_t \partial_n \varphi_1(\mathbf{r}, t) \\ & + \beta_1 \partial_t \tilde{D}'_1[\partial_n \varphi_1](\mathbf{r}, t) - \beta_2 \partial_t \tilde{D}'_2[\partial_n \varphi_1](\mathbf{r}, t) = \beta_1 \partial_t \partial_n \varphi^i(\mathbf{r}, t), \mathbf{r} \in S. \end{aligned} \quad (12)$$

Here, α_k and β_k are real constants.

3 Numerical Solution

To solve the coupled systems of equations Eqs. (5)-(6) and (11)-(12) numerically, first, S is discretized into a mesh of curvilinear triangles and surface unknowns $\varphi_1(\mathbf{r}, t)$ and $\partial_n \varphi_1(\mathbf{r}, t)$ are expanded in space and time as

$$\varphi_1(\mathbf{r}, t) = \sum_{i=1}^{N_t} \sum_{q=1}^{N_p} \sum_{n=1}^{N_n} \mathbf{I}_i^1|_{qn} \vartheta(\mathbf{r}) \ell_{qn}(\mathbf{r}) T(t - i\Delta t), \quad (13)$$

$$\partial_n \varphi_1(\mathbf{r}, t) = \sum_{i=1}^{N_t} \sum_{q=1}^{N_p} \sum_{n=1}^{N_n} \mathbf{I}_i^2|_{qn} \vartheta(\mathbf{r}) \ell_{qn}(\mathbf{r}) T(t - i\Delta t). \quad (14)$$

In Eqs. (13) and (14), N_t is the number of time steps, N_p is the number of curvilinear triangles, N_n is the number of interpolation nodes on each triangle, $\ell_{qn}(\mathbf{r})$ is the Lagrange interpolation function defined at \mathbf{r}_{qn} (node n on triangle q) [28], $\vartheta(\mathbf{r})$ is the inverse of the Jacobian of the coordinate transformation between the unit right triangle and the Cartesian coordinate system, $T(t)$ is the temporal basis function which is constructed using the band-limited approximate prolate spherical wave (APSW) function [43], Δt is the time step size, and $\mathbf{I}_i^1|_{qn}$ and $\mathbf{I}_i^2|_{qn}$ are the unknown expansion coefficients to be solved for.

Substituting Eqs. (13)-(14) into Eqs. (5)-(6) and (11)-(12) and point-testing the resulting equa-

tions in space at \mathbf{r}_{pm} , $p = 1, \dots, N_p$, $m = 1, \dots, N_n$ (i.e., Nyström discretization in space), and in time $t = j\Delta t$ yield the following system of matrix equations

$$\mathbf{Z}_0 \mathbf{I}_j = \mathbf{V}_j - \sum_{i=1}^{j-1} \mathbf{Z}_{j-i} \mathbf{I}_i - \sum_{i=j+1}^{j+N_{\text{hw}}} \mathbf{Z}_{j-i} \mathbf{I}_i, j = 1, \dots, N_t. \quad (15)$$

Here, N_{hw} is the half-width of the APSW function $T(t)$, $\mathbf{I}_j = [\mathbf{I}_j^1 \quad \mathbf{I}_j^2]^T$, where \mathbf{I}_j^1 and \mathbf{I}_j^2 store the unknown expansion coefficients in Eqs. (13) and (14), $\mathbf{V}_j = [\mathbf{V}_j^1 \quad \mathbf{V}_j^2]^T$ store the tested excitation vectors at time $t = j\Delta t$, and

$$\mathbf{Z}_{j-i} = \begin{bmatrix} \mathbf{Z}_{j-i}^{11} & \mathbf{Z}_{j-i}^{12} \\ \mathbf{Z}_{j-i}^{21} & \mathbf{Z}_{j-i}^{22} \end{bmatrix}$$

store the discretized retarded time integrals between nodes of mesh elements. Expressions of elements of \mathbf{V}_j and \mathbf{Z}_{j-i} for TDPIE and TDCPIE are provided in Sections 3.1 and 3.2, respectively. Note that the system of matrix equations in Eq. (15) is not causal, i.e., \mathbf{I}_j can not be solved for without knowing “future” unknowns \mathbf{I}_{j+1} , \mathbf{I}_{j+2} , \dots , $\mathbf{I}_{j+N_{\text{hw}}}$ [see the second summation on the right-hand side of Eq. (15)]. The extrapolation scheme developed in [44] is used here to express these future unknowns \mathbf{I}_{j+1} , \mathbf{I}_{j+2} , \dots , $\mathbf{I}_{j+N_{\text{hw}}}$ in terms of “past/current” unknowns \mathbf{I}_{j-N+1} , \dots , \mathbf{I}_{j-1} , \mathbf{I}_j , where N is the number of samples used in the extrapolation. Inserting this expression into Eq. (15) converts it into a causal form as

$$\bar{\mathbf{Z}}_0 \mathbf{I}_j = \mathbf{V}_j - \sum_{i=1}^{j-1} \bar{\mathbf{Z}}_{j-i} \mathbf{I}_i, j = 1, \dots, N_t. \quad (16)$$

The modified matrices $\bar{\mathbf{Z}}_{j-i}$ in Eq. (16) are obtained from \mathbf{Z}_{j-i} in Eq. (15) using the expressions given in [44]. The system of matrix equations in Eq. (16) is now in a form that can be recursively solved for the unknown coefficient vectors \mathbf{I}_j , $j = 1, \dots, N_t$ via time marching as briefly described next. For $j = 1$, \mathbf{I}_1 is found by solving Eq. (16) with right-hand side \mathbf{V}_1 (contribution from the summation is zero at the first time step). For $j = 2$, the right-hand side of Eq. (16) is computed by subtracting $\bar{\mathbf{Z}}_1 \mathbf{I}_1$ (only term coming from the summation) from \mathbf{V}_2 . Then, \mathbf{I}_2 is found by solving Eq. (16) with this right-hand side. For $j = 3$, the right-hand side of Eq. (16) is computed by

subtracting $\bar{\mathbf{Z}}_2 \mathbf{I}_1 + \bar{\mathbf{Z}}_1 \mathbf{I}_2$ from \mathbf{V}_3 . Then, Eq. (16) is solved for \mathbf{I}_3 . This recursive time marching algorithm is continued until all \mathbf{I}_j , $j = 1, \dots, N_t$ are obtained.

In the next two sections, Sections 3.1 and 3.2, the expressions of the elements of \mathbf{V}_j and \mathbf{Z}_{j-i} in Eq. (15) are provided for TDPIE and TDCPIE, respectively.

3.1 Elements of \mathbf{V}_j and \mathbf{Z}_{j-i} for TDPIE

The elements of \mathbf{V}_j^1 and \mathbf{V}_j^2 are given as $\mathbf{V}_j^1|_{pm} = \partial_t \varphi^i(\mathbf{r}_{pm}, t)|_{t=j\Delta t}$ and $\mathbf{V}_j^2|_{pm} = 0$, respectively.

The elements of \mathbf{Z}_{j-i} are expressed as

$$\begin{aligned}
\mathbf{Z}_{j-i}^{11}|_{pm,qn} &= \frac{1}{2} \vartheta(\mathbf{r}_{pm}) \partial_t T(t)|_{t=(j-i)\Delta t} \delta_{pq} \delta_{mn} \\
&\quad - \partial_t \int_{S_q} \partial_{n'} G_1(R, t) * T(t - i\Delta t) \vartheta(\mathbf{r}') \ell_{qn}(\mathbf{r}') ds' \Big|_{t=j\Delta t}, \\
\mathbf{Z}_{j-i}^{12}|_{pm,qn} &= \partial_t \int_{S_q} G_1(R, t) * T(t - i\Delta t) \vartheta(\mathbf{r}') \ell_{qn}(\mathbf{r}') ds' \Big|_{t=j\Delta t}, \\
\mathbf{Z}_{j-i}^{21}|_{pm,qn} &= \frac{1}{2} \vartheta(\mathbf{r}_{pm}) \partial_t T(t)|_{t=(j-i)\Delta t} \delta_{pq} \delta_{mn} \\
&\quad + \partial_t \int_{S_q} \partial_{n'} G_2(R, t) * T(t - i\Delta t) \vartheta(\mathbf{r}') \ell_{qn}(\mathbf{r}') ds' \Big|_{t=j\Delta t}, \\
\mathbf{Z}_{j-i}^{22}|_{pm,qn} &= -\frac{\rho_2}{\rho_1} \partial_t \int_{S_q} G_2(R, t) * T(t - i\Delta t) \vartheta(\mathbf{r}') \ell_{qn}(\mathbf{r}') ds' \Big|_{t=j\Delta t}. \tag{17}
\end{aligned}$$

Here, $R = |\mathbf{r}_{pm} - \mathbf{r}'|$, S_q is the surface of the curvilinear triangle q , and $\delta_{pq} = 1$ for $p = q$, and $\delta_{pq} = 0$ for $p \neq q$.

3.2 Elements of \mathbf{V}_j and \mathbf{Z}_{j-i} for TDCPIE

The elements of \mathbf{V}_j^1 and \mathbf{V}_j^2 are given as $\mathbf{V}_j^1|_{pm} = \alpha_1 \partial_t \varphi^i(\mathbf{r}_{pm}, t)|_{t=j\Delta t}$ and $\mathbf{V}_j^2|_{pm} = \beta_1 \partial_t \partial_n \varphi^i(\mathbf{r}_{pm}, t)|_{t=j\Delta t}$, respectively. The elements of \mathbf{Z}_{j-i} are expressed as

$$\begin{aligned}
\mathbf{Z}_{j-i}^{11}|_{pm,qn} &= \frac{\alpha_1 + \alpha_2}{2} \vartheta(\mathbf{r}_{pm}) \partial_t T(t)|_{t=(j-i)\Delta t} \delta_{pq} \delta_{mn} \\
&\quad - \alpha_1 \partial_t \int_{S_q} \partial_{n'} G_1(R, t) * T(t - i\Delta t) \vartheta(\mathbf{r}') \ell_{qn}(\mathbf{r}') ds' \Big|_{t=j\Delta t} \\
&\quad + \alpha_2 \partial_t \int_{S_q} \partial_{n'} G_2(R, t) * T(t - i\Delta t) \vartheta(\mathbf{r}') \ell_{qn}(\mathbf{r}') ds' \Big|_{t=j\Delta t}, \\
\mathbf{Z}_{j-i}^{12}|_{pm,qn} &= \alpha_1 \partial_t \int_{S_q} G_1(R, t) * T(t - i\Delta t) \vartheta(\mathbf{r}') \ell_{qn}(\mathbf{r}') ds' \Big|_{t=j\Delta t} \\
&\quad - \alpha_2 \frac{\rho_2}{\rho_1} \partial_t \int_{S_q} G_2(R, t) * T(t - i\Delta t) \vartheta(\mathbf{r}') \ell_{qn}(\mathbf{r}') ds' \Big|_{t=j\Delta t}, \\
\mathbf{Z}_{j-i}^{21}|_{pm,qn} &= -\beta_1 \partial_t \int_{S_q} \partial_{nn'}^2 G_1(R, t) * T(t - i\Delta t) \vartheta(\mathbf{r}') \ell_{qn}(\mathbf{r}') ds' \Big|_{t=j\Delta t} \\
&\quad + \beta_2 \frac{\rho_1}{\rho_2} \partial_t \int_{S_q} \partial_{nn'}^2 G_2(R, t) * T(t - i\Delta t) \vartheta(\mathbf{r}') \ell_{qn}(\mathbf{r}') ds' \Big|_{t=j\Delta t}, \\
\mathbf{Z}_{j-i}^{22}|_{pm,qn} &= \frac{\beta_1 + \beta_2}{2} \vartheta(\mathbf{r}_{pm}) \partial_t T(t)|_{t=(j-i)\Delta t} \delta_{pq} \delta_{mn} \\
&\quad + \beta_1 \partial_t \int_{S_q} \partial_n G_1(R, t) * T(t - i\Delta t) \vartheta(\mathbf{r}') \ell_{qn}(\mathbf{r}') ds' \Big|_{t=j\Delta t} \\
&\quad - \beta_2 \partial_t \int_{S_q} \partial_n G_2(R, t) * T(t - i\Delta t) \vartheta(\mathbf{r}') \ell_{qn}(\mathbf{r}') ds' \Big|_{t=j\Delta t}. \tag{18}
\end{aligned}$$

Computation of the matrix elements in Eqs. (17) and (18) calls for treatment of the singularities of the spatial integrals. This singularity treatment is described in the next section, Section 3.3.

3.3 Computation of Singular Integrals

There are four kinds of integrands in Eqs. (17) and (18): $G_k(R, t) * T(t - i\Delta t)$, $\partial_n G_k(R, t) * T(t - i\Delta t)$, $\partial_{n'} G_k(R, t) * T(t - i\Delta t)$, and $\partial_{nn'}^2 G_k(R, t) * T(t - i\Delta t)$. When $p = q$, and as \mathbf{r}' approaches \mathbf{r}_{pm} , the integrals of $G_k(R, t) * T(t - i\Delta t)$ and $\partial_n G_k(R, t) * T(t - i\Delta t)$ become weakly-singular, the

integral of $\partial_{n'} G_k(R, t) * T(t - i\Delta t)$ becomes strongly-singular, and the integral of $\partial_{nn'}^2 G_k(R, t) * T(t - i\Delta t)$ becomes hyper-singular [45]. The weakly-singular integrals are computed using the Duffy transformation [46]. The strongly-singular integrals in Eq. (17) are computed using the approach described in [29]. The strongly- and hyper-singular integrals in Eq. (18) are computed using the method described as follows.

$T(t - R/c_k)$ is expanded using the Taylor series around $R = 0$ as

$$T(t - R/c_k) = \sum_{u=0}^{\infty} \frac{(-1)^u \partial_t^u T(t)}{u! c_k^u} R^u. \quad (19)$$

Using this expansion in $\partial_{n'}\{T(t - R/c_k)/(4\pi R)\}$ and $\partial_{nn'}^2\{T(t - R/c_k)/(4\pi R)\}$ yields

$$\begin{aligned} \partial_{n'} \frac{T(t - R/c_k)}{4\pi R} &= \frac{(\hat{\mathbf{n}}' \cdot \hat{\mathbf{R}})}{4\pi} \left[\frac{\partial_t T(t - R/c_k)}{c_k R} + \frac{T(t - R/c_k)}{R^2} \right] \\ &= \frac{(\hat{\mathbf{n}}' \cdot \hat{\mathbf{R}})}{4\pi} \left[\sum_{u=0}^{\infty} \frac{(-1)^u \partial_t^{u+1} T(t)}{u! c_k^{u+1}} R^{u-1} + \sum_{u=0}^{\infty} \frac{(-1)^u \partial_t^u T(t)}{u! c_k^u} R^{u-2} \right] \\ &= \frac{(\hat{\mathbf{n}}' \cdot \hat{\mathbf{R}})}{4\pi} \left[\frac{\partial_t T(t)}{c_k} R^{-1} + T(t) R^{-2} + \frac{(-1) \partial_t T(t)}{c_k} R^{-1} + O(R^{u \geq 0}) \right] \\ &= (\hat{\mathbf{n}}' \cdot \hat{\mathbf{R}}) \frac{T(t)}{4\pi R^2} + O(R^{u \geq 0}), \end{aligned} \quad (20)$$

$$\begin{aligned}
\partial_{nn'}^2 \frac{T(t - R/c_k)}{4\pi R} &= \frac{(\hat{\mathbf{n}} \cdot \hat{\mathbf{n}}')}{4\pi} \left[\frac{\partial_t T(t - R/c_k)}{c_k R^2} + \frac{T(t - R/c_k)}{R^3} \right] \\
&\quad - \frac{(\hat{\mathbf{n}} \cdot \hat{\mathbf{R}})(\hat{\mathbf{n}}' \cdot \hat{\mathbf{R}})}{4\pi} \left[\frac{\partial_t^2 T(t - R/c_k)}{c_k^2 R} + \frac{3\partial_t T(t - R/c_k)}{c_k R^2} + \frac{3T(t - R/c_k)}{R^3} \right] \\
&= \frac{(\hat{\mathbf{n}} \cdot \hat{\mathbf{n}}')}{4\pi} \left[\sum_{u=0}^{\infty} \frac{(-1)^u \partial_t^{u+1} T(t)}{u! c_k^{u+1}} R^{u-2} + \sum_{u=0}^{\infty} \frac{(-1)^u \partial_t^u T(t)}{u! c_k^u} R^{u-3} \right] \\
&\quad - \frac{(\hat{\mathbf{n}} \cdot \hat{\mathbf{R}})(\hat{\mathbf{n}}' \cdot \hat{\mathbf{R}})}{4\pi} \left[\sum_{u=0}^{\infty} \frac{(-1)^u \partial_t^{u+2} T(t)}{u! c_k^{u+2}} R^{u-1} + 3 \sum_{u=0}^{\infty} \frac{(-1)^u \partial_t^{u+1} T(t)}{u! c_k^{u+1}} R^{u-2} \right. \\
&\quad \left. + 3 \sum_{u=0}^{\infty} \frac{(-1)^u \partial_t^u T(t)}{u! c_k^u} R^{u-3} \right] \\
&= \frac{(\hat{\mathbf{n}} \cdot \hat{\mathbf{n}}')}{4\pi} \left[\frac{\partial_t T(t)}{c_k} R^{-2} + \frac{(-1) \partial_t^2 T(t)}{c_k^2} R^{-1} + T(t) R^{-3} + \frac{(-1) \partial_t T(t)}{c_k} R^{-2} \right. \\
&\quad \left. + \frac{\partial_t^2 T(t)}{2c_k^2} R^{-1} + O(R^{u \geq 0}) \right] \\
&\quad - \frac{(\hat{\mathbf{n}} \cdot \hat{\mathbf{R}})(\hat{\mathbf{n}}' \cdot \hat{\mathbf{R}})}{4\pi} \left[\frac{\partial_t^2 T(t)}{c_k^2} R^{-1} + 3 \frac{\partial_t T(t)}{c_k} R^{-2} + 3 \frac{(-1) \partial_t^2 T(t)}{c_k^2} R^{-1} \right. \\
&\quad \left. + 3T(t) R^{-3} + 3 \frac{(-1) \partial_t T(t)}{c_k} R^{-2} + 3 \frac{\partial_t^2 T(t)}{2c_k^2} R^{-1} + O(R^{u \geq 0}) \right] \\
&= \left[(\hat{\mathbf{n}} \cdot \hat{\mathbf{n}}') - 3(\hat{\mathbf{n}} \cdot \hat{\mathbf{R}})(\hat{\mathbf{n}}' \cdot \hat{\mathbf{R}}) \right] \frac{T(t)}{4\pi R^3} \\
&\quad + \left[-(\hat{\mathbf{n}} \cdot \hat{\mathbf{n}}') + (\hat{\mathbf{n}} \cdot \hat{\mathbf{R}})(\hat{\mathbf{n}}' \cdot \hat{\mathbf{R}}) \right] \frac{\partial_t^2 T(t)}{8\pi c_k^2 R} + O(R^{u \geq 0}). \tag{21}
\end{aligned}$$

Here, $\hat{\mathbf{R}} = (\mathbf{r}_{pm} - \mathbf{r}')/R$ and $O(R^{u \geq 0})$ represents the higher-order terms that are not singular as $R \rightarrow 0$. The singular terms on the right hands of Eqs. (20) and (21) are subtracted from $\partial_{n'} G_k(R, t) * T(t - i\Delta t)$ and $\partial_{nn'}^2 G_k(R, t) * T(t - i\Delta t)$, respectively. Then, the integrals of these

terms are added back to yield the final expressions for $\mathbf{Z}_{j-i}^{11}|_{pm,qn}$ and $\mathbf{Z}_{j-i}^{21}|_{pm,qn}$ in (18) as

$$\begin{aligned}
\mathbf{Z}_{j-i}^{11}|_{pm,qn} = & -\alpha_1 \partial_t \int_{S_q} \left[\partial_{n'} \frac{T(t-R/c_1)}{4\pi R} - (\hat{\mathbf{n}}' \cdot \hat{\mathbf{R}}) \frac{T(t)}{4\pi R^2} \right] \vartheta(\mathbf{r}') \ell_{qn}(\mathbf{r}') ds' \Big|_{t=(j-i)\Delta t} \\
& - \alpha_1 \int_{S_q} (\hat{\mathbf{n}}' \cdot \hat{\mathbf{R}}) \frac{\partial_t T(t)}{4\pi R^2} \vartheta(\mathbf{r}') \ell_{qn}(\mathbf{r}') ds' \Big|_{t=(j-i)\Delta t} \\
& + \alpha_2 \partial_t \int_{S_q} \left[\partial_{n'} \frac{T(t-R/c_2)}{4\pi R} - (\hat{\mathbf{n}}' \cdot \hat{\mathbf{R}}) \frac{T(t)}{4\pi R^2} \right] \vartheta(\mathbf{r}') \ell_{qn}(\mathbf{r}') ds' \Big|_{t=(j-i)\Delta t} \\
& + \alpha_2 \int_{S_q} (\hat{\mathbf{n}}' \cdot \hat{\mathbf{R}}) \frac{\partial_t T(t)}{4\pi R^2} \vartheta(\mathbf{r}') \ell_{qn}(\mathbf{r}') ds' \Big|_{t=(j-i)\Delta t}, \tag{22}
\end{aligned}$$

$$\begin{aligned}
\mathbf{Z}_{j-i}^{21}|_{pm,qn} = & -\beta_1 \partial_t \int_{S_q} \left\{ \partial_{nn'}^2 \frac{T(t-R/c_1)}{4\pi R} - [(\hat{\mathbf{n}} \cdot \hat{\mathbf{n}}') - 3(\hat{\mathbf{n}} \cdot \hat{\mathbf{R}})(\hat{\mathbf{n}}' \cdot \hat{\mathbf{R}})] \frac{T(t)}{4\pi R^3} \right. \\
& \left. - [-(\hat{\mathbf{n}} \cdot \hat{\mathbf{n}}') + (\hat{\mathbf{n}} \cdot \hat{\mathbf{R}})(\hat{\mathbf{n}}' \cdot \hat{\mathbf{R}})] \frac{\partial_t^2 T(t)}{8\pi c_1^2 R} \right\} \vartheta(\mathbf{r}') \ell_{qn}(\mathbf{r}') ds' \Big|_{t=(j-i)\Delta t} \\
& - \beta_1 \int_{S_q} [(\hat{\mathbf{n}} \cdot \hat{\mathbf{n}}') - 3(\hat{\mathbf{n}} \cdot \hat{\mathbf{R}})(\hat{\mathbf{n}}' \cdot \hat{\mathbf{R}})] \frac{\partial_t T(t)}{4\pi R^3} \vartheta(\mathbf{r}') \ell_{qn}(\mathbf{r}') ds' \Big|_{t=(j-i)\Delta t} \\
& - \beta_1 \int_{S_q} [-(\hat{\mathbf{n}} \cdot \hat{\mathbf{n}}') + (\hat{\mathbf{n}} \cdot \hat{\mathbf{R}})(\hat{\mathbf{n}}' \cdot \hat{\mathbf{R}})] \frac{\partial_t^3 T(t)}{8\pi c_1^2 R} \vartheta(\mathbf{r}') \ell_{qn}(\mathbf{r}') ds' \Big|_{t=(j-i)\Delta t} \\
& + \beta_2 \frac{\rho_1}{\rho_2} \partial_t \int_{S_q} \left\{ \partial_{nn'}^2 \frac{T(t-R/c_2)}{4\pi R} - [(\hat{\mathbf{n}} \cdot \hat{\mathbf{n}}') - 3(\hat{\mathbf{n}} \cdot \hat{\mathbf{R}})(\hat{\mathbf{n}}' \cdot \hat{\mathbf{R}})] \frac{T(t)}{4\pi R^3} \right. \\
& \left. - [-(\hat{\mathbf{n}} \cdot \hat{\mathbf{n}}') + (\hat{\mathbf{n}} \cdot \hat{\mathbf{R}})(\hat{\mathbf{n}}' \cdot \hat{\mathbf{R}})] \frac{\partial_t^2 T(t)}{8\pi c_2^2 R} \right\} \vartheta(\mathbf{r}') \ell_{qn}(\mathbf{r}') ds' \Big|_{t=(j-i)\Delta t} \\
& + \beta_2 \frac{\rho_1}{\rho_2} \int_{S_q} [(\hat{\mathbf{n}} \cdot \hat{\mathbf{n}}') - 3(\hat{\mathbf{n}} \cdot \hat{\mathbf{R}})(\hat{\mathbf{n}}' \cdot \hat{\mathbf{R}})] \frac{\partial_t T(t)}{4\pi R^3} \vartheta(\mathbf{r}') \ell_{qn}(\mathbf{r}') ds' \Big|_{t=(j-i)\Delta t} \\
& + \beta_2 \frac{\rho_1}{\rho_2} \int_{S_q} [-(\hat{\mathbf{n}} \cdot \hat{\mathbf{n}}') + (\hat{\mathbf{n}} \cdot \hat{\mathbf{R}})(\hat{\mathbf{n}}' \cdot \hat{\mathbf{R}})] \frac{\partial_t^3 T(t)}{8\pi c_2^2 R} \vartheta(\mathbf{r}') \ell_{qn}(\mathbf{r}') ds' \Big|_{t=(j-i)\Delta t}. \tag{23}
\end{aligned}$$

The first and the third integrals on the right-hand side of Eq. (22) and the first and the fourth integrals on the right-hand side of Eq. (23) are “smooth” and computed using a Gaussian quadrature rule [47]. The third and the sixth integrals on the right-hand side of Eq. (23) are weakly-singular and computed using the Duffy transformation [46]. The second and the fourth integrals on the

right-hand side of Eq. (22) and the second and the fifth integrals on the right-hand side of Eq. (23) cancel out each other for $\alpha_1 = \alpha_2$ and $\beta_1\rho_2 = \beta_2\rho_1$, respectively.

4 Numerical Results

In this section, numerical results, which demonstrate the relationship between numerical errors and interior resonance modes, are presented. TDPIE and TDCPIE are used to analyze acoustic scattering from a penetrable unit sphere that resides in an unbounded background medium. It is assumed that the sphere is centered at the origin. The wave speed in the background medium and inside the sphere is $c_1 = 300$ m/s and $c_2 = 200$ m/s, respectively. The ratio of the densities in these two media is $\rho_1/\rho_2 = 1.5$. In all simulations, the excitation is a plane wave with velocity potential

$$\varphi^i(\mathbf{r}, t) = \varphi_0 G(t - \hat{\mathbf{k}}^i \cdot \mathbf{r}/c_1), \quad (24)$$

where φ_0 is the amplitude, $\hat{\mathbf{k}}^i$ is the unit vector along the direction of propagation, and $G(t) = \cos[2\pi f_0(t - t_p)] \exp[-(t - t_p)^2/(2\sigma^2)]$ is a modulated Gaussian pulse with center frequency f_0 , time delay t_p , and duration σ . The excitation parameters are selected as $\varphi_0 = 1$ m²/s, $\hat{\mathbf{k}}^i = \hat{\mathbf{z}}$, $f_0 = 120$ Hz, $t_p = 10\sigma$, and $\sigma = 3/(2\pi f_{\text{bw}})$, where the effective bandwidth $f_{\text{bw}} = 80$ Hz. Note that this definition of σ ensures that 99.997% of the wave energy is within the frequency band $[f_{\text{min}}, f_{\text{max}}]$ with $f_{\text{min}} = f_0 - f_{\text{bw}}$ and $f_{\text{max}} = f_0 + f_{\text{bw}}$ [48]. Also, this specific selection of $f_0 = 120$ Hz and $f_{\text{bw}} = 80$ Hz ensures that the frequency of the lowest interior resonance mode (the first cavity mode of the Dirichlet problem), 150 Hz, is within the frequency band $[f_{\text{min}}, f_{\text{max}}]$, i.e., this resonance mode could possibly be excited using the Gaussian pulse described above [14]. The time step size is chosen as $\Delta t = 1/(2\gamma f_{\text{max}})$ with oversampling factor γ . The half-width of the APSW interpolator used to construct $T(t)$ is $N_{\text{hw}} = 7$. The surface of the sphere is discretized using $N_p = 396$ curvilinear triangles with $N_n = 6$ interpolation nodes on each triangle. For TDCPIE, the linear combination coefficients in Eqs. (11) and (12) are chosen as $\alpha_1 = \alpha_2 = \beta_1 = 1$ and $\beta_2 = 2/3$. LU decomposition is used to solve the matrix system in Eq. (16) (at every time step) to ensure that the error in the matrix solution is at the machine precision level [49].

4.1 Accuracy of TDPIE and TDCPIE

For the first set of simulations, the oversampling factor is selected as $\gamma = 6$ resulting in $\Delta t = 0.42$ ms. 16-point Gaussian and 9-point Gauss-Legendre quadrature rules [47] are used to compute the two-dimensional (2D) surface integral with “smooth” integrand and the one-dimensional (1D) line integral needed for the Duffy transformation [46], respectively. Fig. 2 compares the magnitude of the expansion coefficient $\mathbf{I}_j^1 \Big|_{qn}$, $q = 3$, $n = 3$ (corresponding to $\mathbf{r}_{qn} = (0.78, 0.58, 0.23)$ m), $j = 1, \dots, N_t$ computed by solving TDPIE with that computed by solving TDCPIE. Clearly, the solution of TDPIE is corrupted by non-decaying oscillations while the solution of TDCPIE is free from any resonances. Fig. 3 shows the normalized Fourier transform of $\varphi_1(\mathbf{r}, t)$ [i.e., Fourier transform of $\varphi_1(\mathbf{r}, t)$ divided by the Fourier transform of $G(t)$] computed after solving TDPIE and TDCPIE and compares that to the frequency-domain (time-harmonic) total velocity potential computed at $\mathbf{r} = (0.78, 0.58, 0.23)$ m using the Mie series solution [50]. Note that the normalization is required to ensure that the time-harmonic response (with equal excitation amplitude at each frequency) is obtained from the solutions of TDPIE and TDCPIE. Fig. 3 clearly shows that both simulations are accurate within the effective band of the excitation, except at 150 Hz where the solution of TDPIE is corrupted by the interior resonance mode. Fig. 3 also shows that TDPIE is more accurate than TDCPIE at other frequencies. This might be explained by the fact that a second-kind surface integral equation (e.g., TDCPIE) is usually less accurate than its first-kind counterpart (e.g., TDPIE) [51].

The effect of interior resonances on the scattered velocity potential is investigated by comparing the scattering cross section (SCS) of the sphere computed using the normalized Fourier transformed solutions of TDPIE and TDCPIE to SCS computed using the Mie series solution [50]. Fig. 4(a) and (b) plot SCS versus θ for $\phi = 0^\circ$ at 120 Hz and 150 Hz, respectively. As shown in Fig. 4(a), SCS computed using TDPIE and TDCPIE solutions at 120 Hz shows good agreement with the Mie results. On the other hand, as shown in Fig. 4(b), the resonance mode at 150 Hz dramatically changes SCS computed using the TDPIE solution.

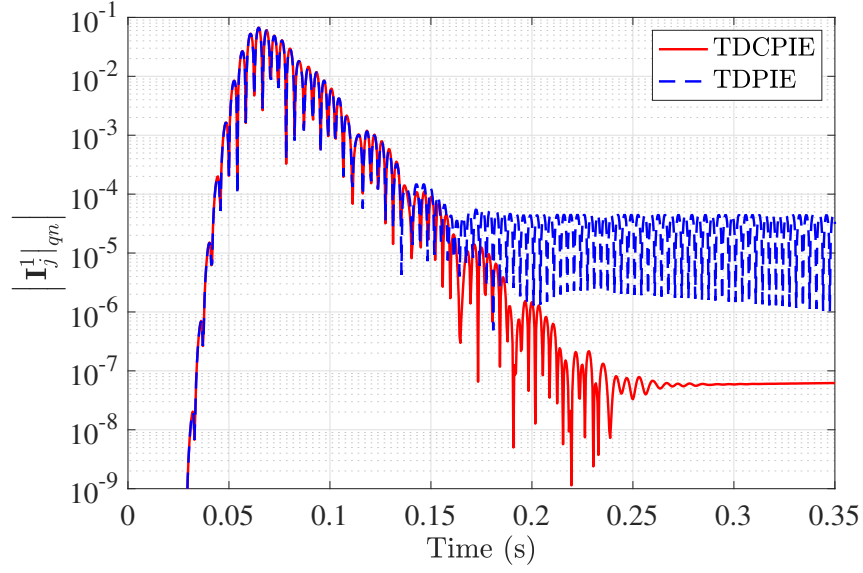


Figure 2: Magnitude of the expansion coefficient $\mathbf{I}_j^1|_{qn}$, $q = 3$, $n = 3$ (corresponding to $\mathbf{r}_{qn} = (0.78, 0.58, 0.23)$ m), $j = 1, \dots, N_t$ computed by solving TDPIE and TDCPIE.

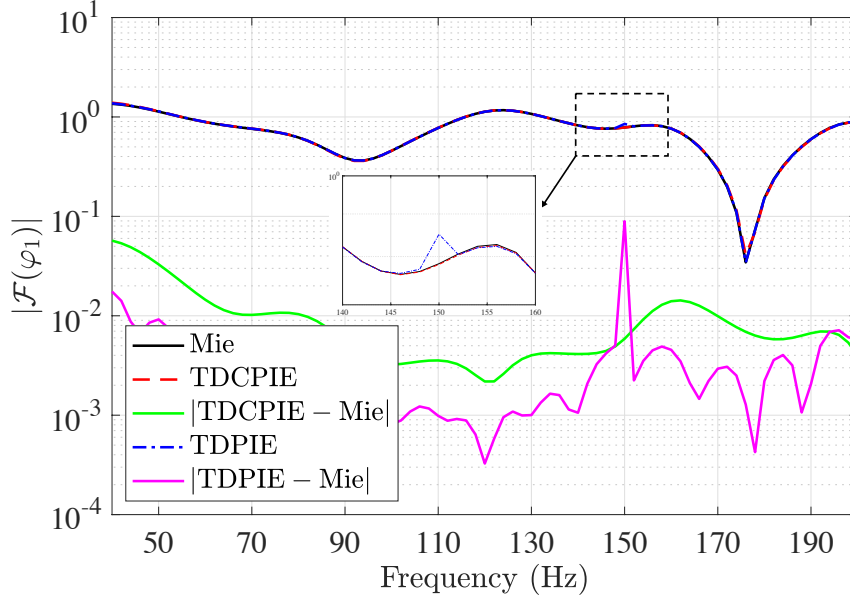
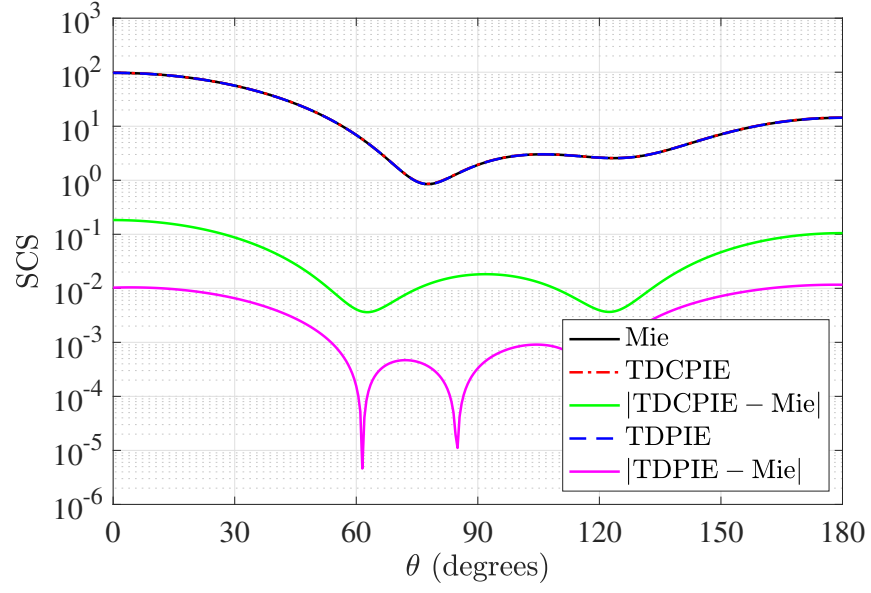
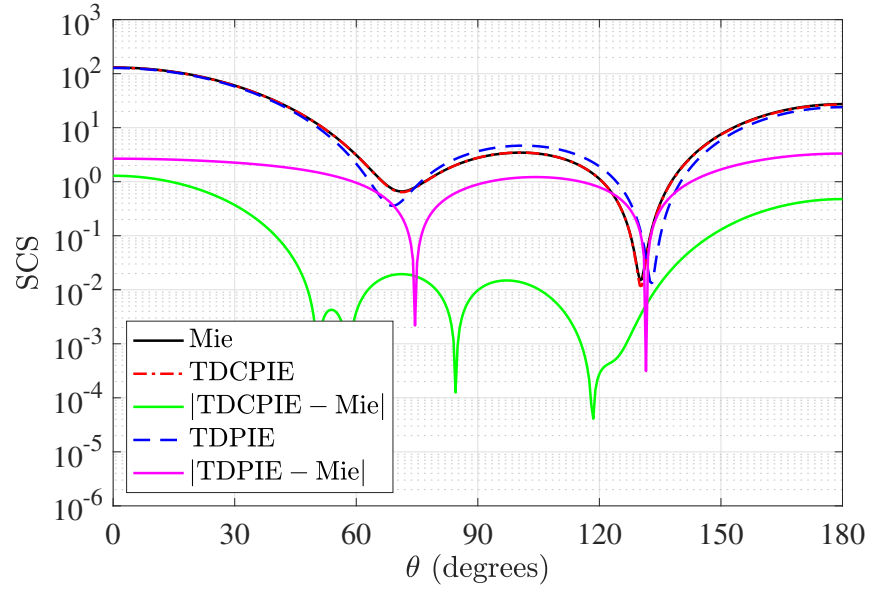


Figure 3: Normalized Fourier transform of $\varphi_1(\mathbf{r}, t)$ computed after solving TDPIE and TDCPIE and the frequency-domain total velocity potential computed at $\mathbf{r} = (0.78, 0.58, 0.23)$ m using the Mie series.



(a)



(b)

Figure 4: SCS computed using the Fourier transformed solutions of TDCPIE and TDPIE and the Mie series solution versus θ for $\phi = 0^\circ$ at (a) 120 Hz and (b) 150 Hz.

4.2 Effect of Numerical Integration Accuracy

In this set of simulations, the effect of the computation accuracy of the integrals in Eqs. (17) and (18) on the amplitude of the interior resonance modes is investigated. Three sets of computation accuracy are considered by using different number of quadrature points to compute the 2D surface integral with “smooth” integrand and the 1D line integral needed for the Duffy transformation [46]:

- (i) 16-point Gaussian and 9-point Gauss-Legendre quadrature rules
- (ii) 7-point Gaussian and 5-point Gauss-Legendre quadrature rules
- (iii) 4-point Gaussian and 3-point Gauss-Legendre quadrature rules

In all simulations, the oversampling factor is selected as $\gamma = 6$ resulting in $\Delta t = 0.42$ ms. To clearly identify the interior resonance mode, Fourier transforms of the late-time data of $\mathbf{I}_j^1|_{qn}$, $q = 3$, $n = 3$ (corresponding to $\mathbf{r}_{qn} = (0.78, 0.58, 0.23)$ m) computed after solving TDCPIE and TDPIE with integration accuracy sets (i), (ii), and (iii) in the time range $t \in [0.8 \text{ s}, 1 \text{ s}]$ are plotted in Fig. 5. The figure shows that the solutions of TDPIE with all three sets exhibit spurious interior resonance mode at 150 Hz. However, as expected, no spurious resonance mode is present in the solutions of TDCPIE. Furthermore, the amplitude of the interior resonance mode observed in the solution of TDPIE with set (iii) is stronger than those with sets (i) and (ii). This is because set (iii) yields larger numerical errors than sets (i) and (ii).

To compare the accuracy of the solutions of TDCPIE and TDPIE with sets (i), (ii), and (iii), the L_2 -norm error in the normalized Fourier transform of $\varphi_1(\mathbf{r}, t)$ (over all 2376 interpolation nodes on the sphere surface) and the L_2 -norm error in SCS (for $\theta = [0^\circ, 180^\circ]$ with 361 sample points and $\phi = 0^\circ$) are plotted versus frequency in Fig. 6(a) and (b), respectively. Note that the reference data used in the computation of the L_2 -norm errors is obtained using the Mie series solution. Fig. 6 shows that the accuracy of the TDPIE solution in the vicinity of 150 Hz is significantly affected by the interior resonance mode. As expected, larger numerical errors increase the amplitude of the resonance mode. Fig. 6 also shows that the spurious interior resonance mode is not observed in the TDCPIE solution regardless of the integral computation accuracy.

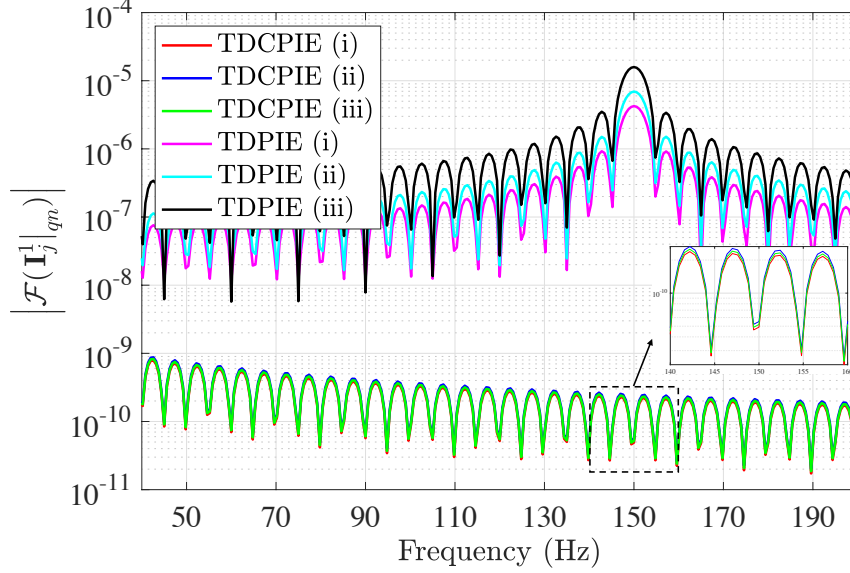
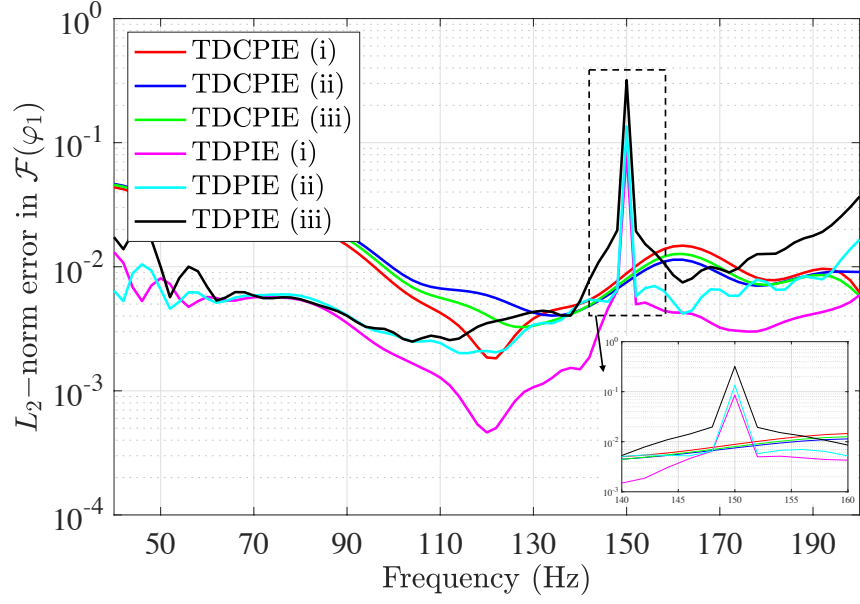


Figure 5: Fourier transforms of $\mathbf{I}_j^1|_{qn}$, $q = 3$, $n = 3$ (corresponding to $\mathbf{r}_{qn} = (0.78, 0.58, 0.23)$ m) computed after solving TDCPIE and TDPIE with the integration accuracy sets (i), (ii), and (iii) in the time range $t \in [0.8 \text{ s}, 1 \text{ s}]$.

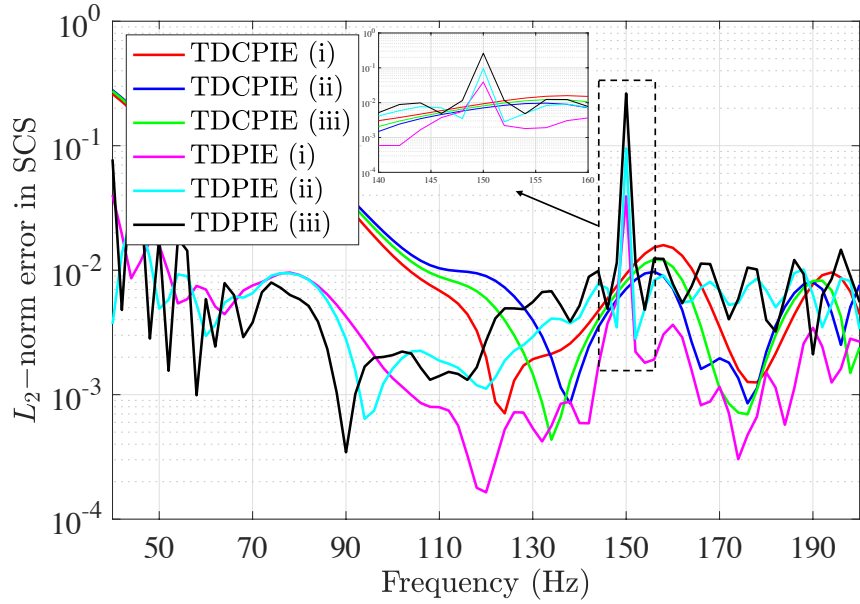
To visualize the interior resonance mode at 150 Hz, the normalized Fourier transform of $\varphi_1(\mathbf{r}, t)$ (at all interpolation nodes on the sphere surface) computed after solving TDCPIE and TDPIE with set (iii) are presented in Fig. 7(a) and (b), respectively. Fig. 7(c) presents the difference in the normalized Fourier transform of $\varphi_1(\mathbf{r}, t)$ obtained from the TDCPIE and TDPIE solutions. As expected, the pattern of the difference follows the amplitude of the interior resonance mode [52].

4.3 Effect of Time Step Size

In this set of simulations, the effect of time step size Δt (i.e., temporal discretization density) on the amplitude of the interior resonance modes is demonstrated. Three different oversampling factors are used: $\gamma \in \{6, 7.5, 10\}$ resulting in $\Delta t = \{0.42, 0.33, 0.25\}$ ms, respectively. In all simulations, the integration accuracy set (i) described in Section 4.2 is used to ensure that the numerical error resulting from the computation of the space integrals in matrix elements is suppressed to be sufficiently small. Fig. 8 plots the Fourier transforms of $\mathbf{I}_j^1|_{qn}$, $q = 3$, $n = 3$ (corresponding to $\mathbf{r}_{qn} = (0.78, 0.58, 0.23)$ m) computed after solving TDCPIE and TDPIE with $\gamma = 6$, $\gamma = 7.5$, and $\gamma = 10$ in the time range $t \in [0.8 \text{ s}, 1 \text{ s}]$. As expected, interior resonance mode is observed in the



(a)



(b)

Figure 6: L_2 -norm error (a) in the normalized Fourier transform of $\varphi_1(\mathbf{r}, t)$ (at all the interpolation nodes on the sphere surface) and (b) in SCS for $\theta = [0^\circ, 180^\circ]$ and $\phi = 0^\circ$ (at 361 samples points) computed after solving TDCPIE and TDPIE with the integration accuracy sets (i), (ii), and (iii).

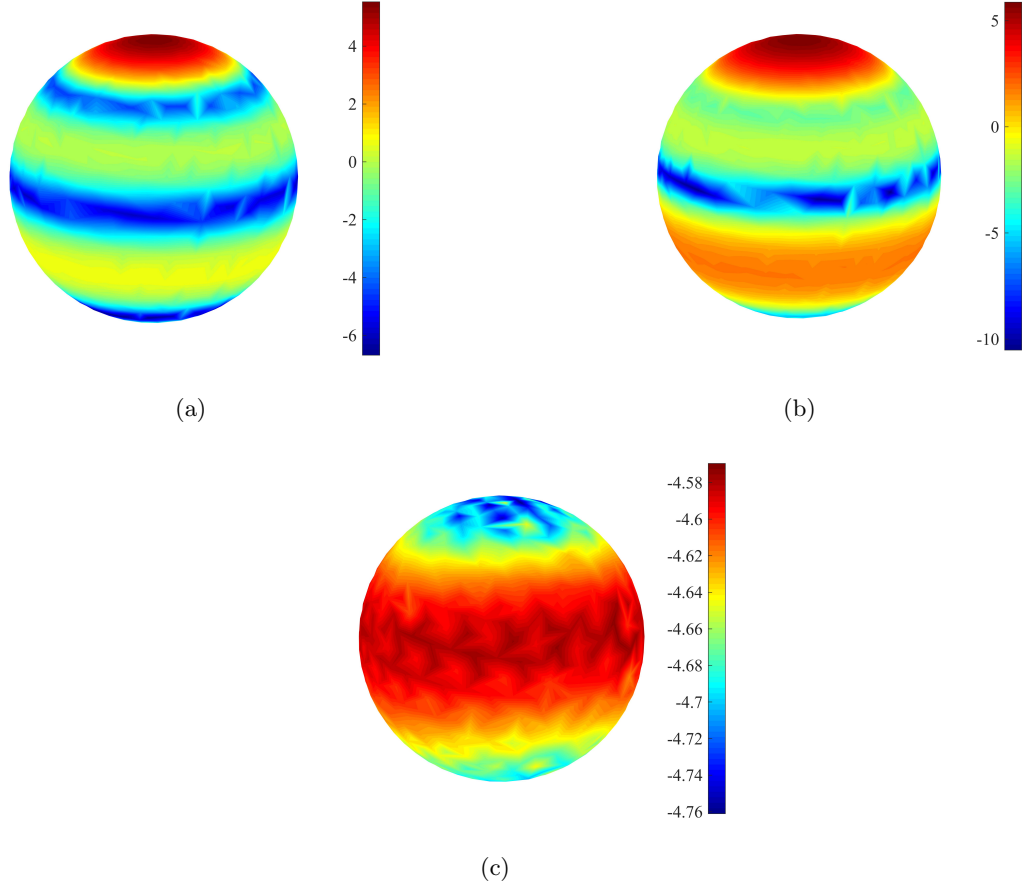


Figure 7: Patterns of the normalized Fourier transform of $\varphi_1(\mathbf{r}, t)$ over the sphere surface at 150 Hz. (a) TDCPIE solution. (b) TDPIE solution. (c) Difference between TDCPIE and TDPIE solutions.

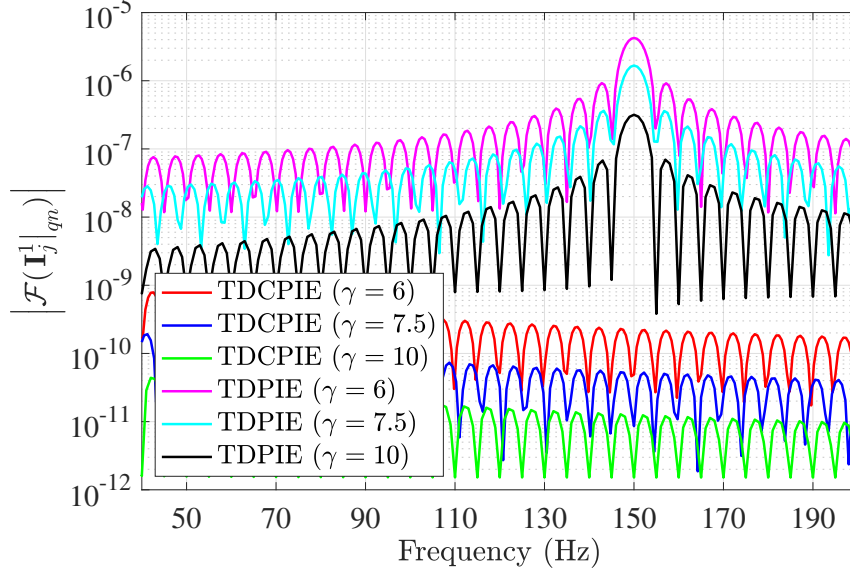
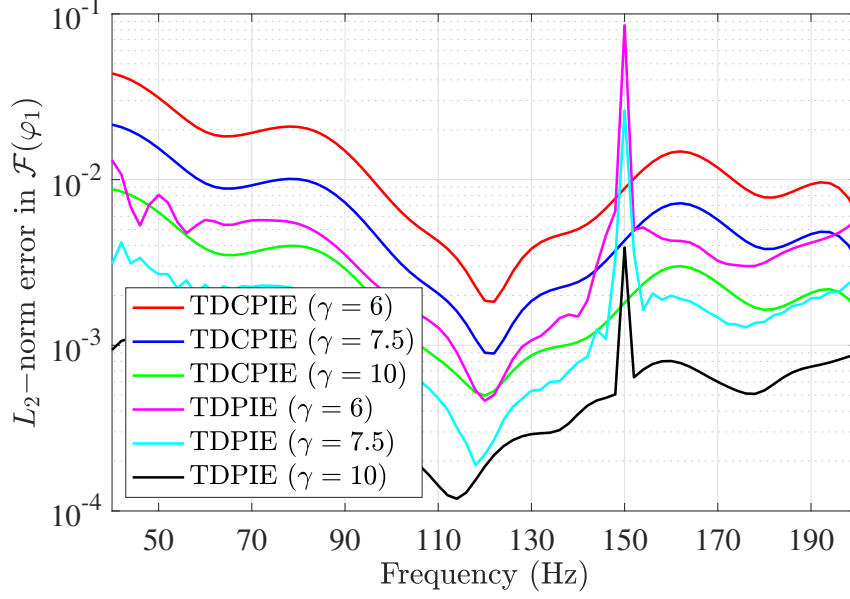
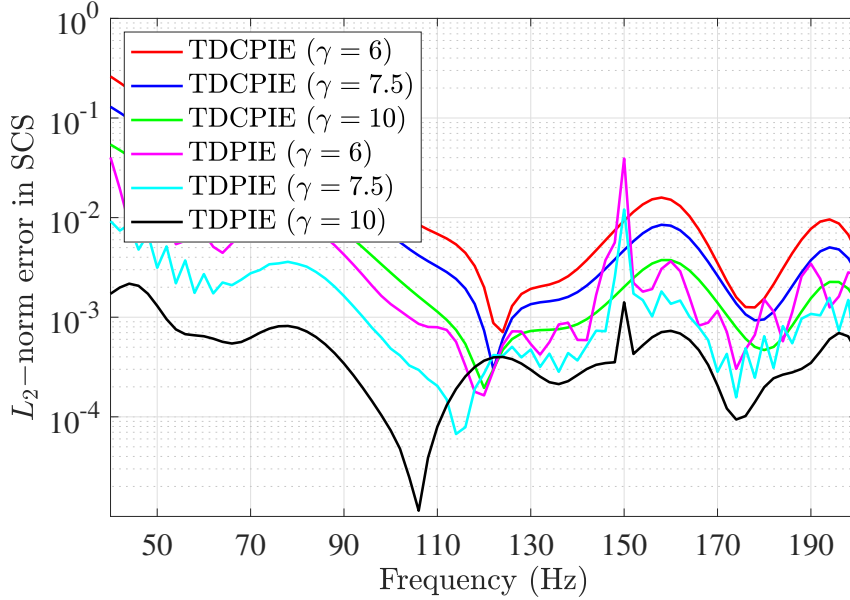


Figure 8: Fourier transforms of $\mathbf{I}_j^1|_{qn}$, $q = 3$, $n = 3$ (corresponding to $\mathbf{r}_{qn} = (0.78, 0.58, 0.23) \text{ m}$) computed after solving TDCPIE and TDPIE with $\gamma = 6$, $\gamma = 7.5$, and $\gamma = 10$ in the time range $t \in [0.8 \text{ s}, 1 \text{ s}]$.

TDPIE solution at 150 Hz. Furthermore, the figure shows that using a larger γ (or smaller Δt) reduces the amplitude of the resonance mode. As expected, no interior resonance mode is observed in the TDCPIE solution regardless of the value of γ used. Fig. 9(a) and (b) plot the L_2 -norm error in the normalized Fourier transform of $\varphi_1(\mathbf{r}, t)$ (over all 2376 interpolation nodes on the sphere surface) and the L_2 -norm error in SCS (for $\theta = [0^\circ, 180^\circ]$ at 361 sample points and $\phi = 0^\circ$) computed after solving TDCPIE and TDPIE with $\gamma = 6$, $\gamma = 7.5$, and $\gamma = 10$, respectively. Note that the reference data used in the computation of the L_2 -norm errors is obtained using the Mie series solution. Fig. 9 shows that interior resonance mode is observed in all of the TDPIE solutions with different γ but its amplitude could be significantly suppressed by increasing γ . Another point to note here is that, even though the TDCPIE solution does not admit any interior resonance modes, it is usually less accurate than the TDPIE solution within the whole effective band of the excitation except in the vicinity of 150 Hz.



(a)



(b)

Figure 9: L_2 -norm error (a) in the normalized Fourier transform of $\varphi_1(\mathbf{r}, t)$ (at all the interpolation nodes on the sphere surface) and (b) in SCS for $\theta = [0^\circ, 180^\circ]$ and $\phi = 0^\circ$ (at 361 sample points) computed after solving TDCPIE and TDPIE with $\gamma = 6$, $\gamma = 7.5$, and $\gamma = 10$.

5 Conclusion

The interior resonance problem of TDPIE and TDCPIE that are formulated to analyze the time domain acoustic field interactions on penetrable scatterers is investigated. Numerical results demonstrate that the solution of TDPIE is corrupted by the spurious interior resonance modes that oscillate (without any decay) with the resonance frequencies of the acoustic cavity in the shape of the scatterer and has the density and the wave speed of the background medium. However, unlike the frequency-domain integral equations, the amplitude of these modes in the time domain can be suppressed by reducing the numerical error. On the other hand, the solution of TDCPIE, which is obtained by linearly combining TDPIE with its normal derivative, is free from spurious interior resonance modes. It should be noted here that the weights of this linear combination are carefully selected to enable the numerical computation of the singular integrals.

Acknowledgements

This publication is based upon work supported by the King Abdullah University of Science and Technology (KAUST) Office of Sponsored Research (OSR) under Award No 2019-CRG8-4056. The authors would like to thank the King Abdullah University of Science and Technology Supercomputing Laboratory (KSL) for providing the required computational resources.

References

- [1] J. D. Gonzalez, E. F. Lavia, S. Blanc, M. Maas, and A. Madirolas, “Boundary element method to analyze acoustic scattering from a coupled swimbladder-fish body configuration,” *J. Sound Vib.*, vol. 486, p. 115609, 2020.
- [2] M. A. S. Pessôa and A. A. R. Neves, “Acoustic scattering and forces on an arbitrarily sized fluid sphere by a general acoustic field,” *J. Sound Vib.*, vol. 479, p. 115373, 2020.

- [3] A. M. Prospathopoulos, G. A. Athanassoulis, and K. A. Belibassakis, “Underwater acoustic scattering from a radially layered cylindrical obstacle in a 3D ocean waveguide,” *J. Sound Vib.*, vol. 319, no. 3-5, pp. 1285–1300, 2009.
- [4] Y. I. Bobrovitskii, “A new impedance-based approach to analysis and control of sound scattering,” *J. Sound Vib.*, vol. 297, no. 3-5, pp. 743–760, 2006.
- [5] R. Kittappa and R. Kleinman, “Acoustic scattering by penetrable homogeneous objects,” *J. Math. Phys.*, vol. 16, pp. 421–432, Feb. 1975.
- [6] D. C. Thomas, K. L. Gee, and R. S. Turley, “A balloon lens: Acoustic scattering from a penetrable sphere,” *AM. J. Phys.*, vol. 77, pp. 197–203, Mar. 2009.
- [7] R. E. Kleinman and P. A. Martin, “On single integral equations for the transmission problem of acoustics,” *SIAM J. Appl. Math.*, vol. 48, pp. 307–325, Apr. 1988.
- [8] M. Costabel and E. Stephan, “A direct boundary integral equation method for transmission problems,” *J. Math. Anal. Appl.*, vol. 106, no. 2, pp. 367–413, 1985.
- [9] R. Kress and G. Roach, “Transmission problems for the Helmholtz equation,” *J. Math. Phys.*, vol. 19, no. 6, pp. 1433–1437, 1978.
- [10] H. Wu, Y. Liu, and W. Jiang, “A fast multipole boundary element method for 3D multi-domain acoustic scattering problems based on the Burton–Miller formulation,” *Eng. Anal. Bound Elem.*, vol. 36, no. 5, pp. 779–788, 2012.
- [11] D. Colton and R. Kress, *Integral Equation Methods in Scattering Theory*. New York: Wiley, 1984.
- [12] H. A. Schenck, “Improved integral formulation for acoustic radiation problems,” *J. Acoust. Soc. Am.*, vol. 44, pp. 41–58, Jul. 1968.
- [13] A. J. Burton and G. F. Miller, “The application of integral equation methods to the numerical solution of some exterior boundary-value problems,” *Proc. R. Soc. London Ser. A*, vol. 323, pp. 201–210, Jun. 1971.

- [14] C.-J. Zheng, H.-B. Chen, H.-F. Gao, and L. Du, “Is the Burton–Miller formulation really free of fictitious eigenfrequencies?,” *Eng. Anal. Bound Elem.*, vol. 59, pp. 43–51, Oct. 2015.
- [15] E. Schulz and R. Hiptmair, “Spurious resonances in coupled domain-boundary variational formulations of transmission problems in electromagnetism and acoustics,” *arXiv preprint arXiv:2003.14357*, 2020.
- [16] A. Buffa and R. Hiptmair, “Regularized combined field integral equations,” *Numer. Math.*, vol. 100, no. 1, pp. 1–19, 2005.
- [17] Y. Boubendir, V. Dominguez, D. Levadoux, and C. Turc, “Regularized combined field integral equations for acoustic transmission problems,” *SIAM J. Appl. Math.*, vol. 75, no. 3, pp. 929–952, 2015.
- [18] D. Jones, “Integral equations for the exterior acoustic problem,” *Quarterly J. Mech. Appl. Math.*, vol. 27, no. 1, pp. 129–142, 1974.
- [19] J.-Y. Hwang and S.-C. Chang, “A retracted boundary integral equation for exterior acoustic problem with unique solution for all wave numbers,” *J. Acoust. Soc. Am.*, vol. 90, no. 2, pp. 1167–1180, 1991.
- [20] Z. Y. Qian, Z. D. Han, P. Ufimtsev, and S. N. Atluri, “Non-hyper-singular boundary integral equations for acoustic problems, implemented by the collocation-based boundary element method,” *Comput. Model. Eng. Sci.*, vol. 6, pp. 133–144, 2004.
- [21] A. Ergin, B. Shanker, and E. Michielssen, “Analysis of transient wave scattering from rigid bodies using a Burton–Miller approach,” *J. Acoust. Soc. Am.*, vol. 106, pp. 2396–2404, Nov. 1999.
- [22] D. J. Chappell, P. J. Harris, D. Henwood, and R. Chakrabarti, “A stable boundary element method for modeling transient acoustic radiation,” *J. Acoust. Soc. Am.*, vol. 120, no. 1, pp. 74–80, 2006.

- [23] H.-W. Jang and J.-G. Ih, “Stabilization of time domain acoustic boundary element method for the exterior problem avoiding the nonuniqueness,” *J. Acoust. Soc. Am.*, vol. 133, no. 3, pp. 1237–1244, 2013.
- [24] J. H. Kao, “A time-shifting algorithm for alleviating convergence difficulties at interior acoustic resonance frequencies,” *Appl. Sci.*, vol. 11, no. 6, p. 2701, 2021.
- [25] Y. Shi, H. Bagci, and M. Lu, “On the internal resonant modes in marching-on-in-time solution of the time domain electric field integral equation,” *IEEE Trans. Antennas Propag.*, vol. 61, pp. 4389–4392, Aug. 2013.
- [26] B. Shanker, A. A. Ergin, K. Aygun, and E. Michielssen, “Analysis of transient electromagnetic scattering from closed surfaces using a combined field integral equation,” *IEEE Trans. Antennas Propag.*, vol. 48, pp. 1064–1074, Jul. 2000.
- [27] J. Li, D. Dault, and B. Shanker, “A quasianalytical time domain solution for scattering from a homogeneous sphere,” *J. Acoust. Soc. Am.*, vol. 135, pp. 1676–1685, Apr. 2014.
- [28] G. Kang, J. Song, W. C. Chew, K. C. Donepudi, and J.-M. Jin, “A novel grid-robust higher order vector basis function for the method of moments,” *IEEE Trans. Antennas Propag.*, vol. 49, pp. 908–915, Jun. 2001.
- [29] R. Chen, S. B. Sayed, N. Alharthi, D. Keyes, and H. Bagci, “An explicit marching-on-in-time scheme for solving the time domain Kirchhoff integral equation,” *J. Acoust. Soc. Am.*, vol. 146, pp. 2068–2079, Sep. 2019.
- [30] R. Chen, S. B. Sayed, H. A. Ulku, and H. Bagci, “An explicit time marching scheme for efficient solution of the magnetic field integral equation at low frequencies,” *IEEE Trans. Antennas Propag.*, vol. 69, pp. 1213–1218, Feb. 2021.
- [31] R. Chen and H. Bagci, “On higher-order Nyström discretization of scalar potential integral equation for penetrable scatterers,” in *Proc. Appl. Comput. Electromagn. Symp.*, (Miami, FL, USA), pp. 1–2, Apr. 2019.

- [32] R. Chen and H. Bagci, “Explicit solution of time domain scalar potential surface integral equations for penetrable scatterers,” in *Proc. IEEE Int. Symp. Antennas Propag. USNC/URSI Nat. Radio Sci. Meeting*, (Montreal, Canada), pp. 1001–1002, Jul. 2020.
- [33] R. Chen, *Transient Analysis of Electromagnetic and Acoustic Scattering using Second-kind Surface Integral Equations*. PhD thesis, King Abdullah University of Science and Technology, Thuwal, Saudi Arabia, Apr. 2021.
- [34] R. Chen and H. Bagci, “An explicit MOT scheme for solving the Nyström-discretized TD-MFIE,” in *Proc. IEEE Int. Symp. Antennas Propag. USNC/URSI Nat. Radio Sci. Meeting*, (Boston, MA, USA), pp. 2443–2444, Jul. 2018.
- [35] R. Chen and H. Bagci, “A higher-order explicit marching-on-in-time for analysis of transient acoustic scattering from rigid objects,” in *Proc. IEEE Int. Symp. Antennas Propag. USNC/URSI Nat. Radio Sci. Meeting*, (Atlanta, GA, USA), pp. 179–180, Jul. 2019.
- [36] R. Chen, S. B. Sayed, and H. Bagci, “An explicit marching-on-in-time scheme for solving the Kirchhoff integral equation,” in *Proc. IEEE Int. Symp. Antennas Propag. USNC/URSI Nat. Radio Sci. Meeting*, (Boston, MA, USA), pp. 2409–2410, Jul. 2018.
- [37] M. Abduljabbar, M. A. Farhan, N. Al-Harhi, R. Chen, R. Yokota, H. Bagci, and D. Keyes, “Extreme scale FMM-accelerated boundary integral equation solver for wave scattering,” *SIAM J. Sci. Comput.*, vol. 41, no. 3, pp. C245–C268, 2019.
- [38] N. Al-Harhi, R. Alomairy, K. Akbudak, R. Chen, H. Ltaief, H. Bagci, and D. Keyes, “Solving acoustic boundary integral equations using high performance tile low-rank LU factorization,” in *Proc. Int. Conf. High Perform. Comput.*, (Frankfurt, Germany), pp. 209–229, Jun. 2020.
- [39] R. Chen and H. Bagci, “An explicit time marching scheme to solve surface integral equations for acoustically penetrable scatterers,” in *Proc. URSI Gen. Assem. Sci. Symp.*, (Rome, Italy), Aug. 2020.

- [40] N. Alharthi, R. Chen, H. Bagci, and D. Keyes, “A comparative study of singularity treatment schemes in higher-order Nyström method for acoustic scattering,” in *Proc. URSI Gen. Assem. Sci. Symp.*, (Montreal, Canada), Aug. 2017.
- [41] A. D. Pierce, *Acoustics: An Introduction to Its Physical Principles and Applications*. New York: McGraw-Hill, 1981.
- [42] A. Ishimaru, *Electromagnetic Wave Propagation, Radiation, and Scattering*. Upper Saddle River, NJ: Prentice Hall, 1990.
- [43] J. Knab, “Interpolation of band-limited functions using the approximate prolate series (Corresp.),” *IEEE Trans. Inform. Theory*, vol. 25, pp. 717–720, Nov. 1979.
- [44] S. B. Sayed, H. A. Ulku, and H. Bagci, “A stable marching on-in-time scheme for solving the time-domain electric field volume integral equation on high-contrast scatterers,” *IEEE Trans. Antennas Propag.*, vol. 63, pp. 3098–3110, May 2015.
- [45] Y. Liu and F. J. Rizzo, “A weakly singular form of the hypersingular boundary integral equation applied to 3-D acoustic wave problems,” *Comput. Methods Appl. Mech. Eng.*, vol. 96, no. 2, pp. 271–287, 1992.
- [46] M. G. Duffy, “Quadrature over a pyramid or cube of integrands with a singularity at a vertex,” *SIAM J. Numer. Anal.*, vol. 19, pp. 1260–1262, Dec. 1982.
- [47] J.-M. Jin, *Theory and Computation of Electromagnetic Fields*. Hoboken, NJ: Wiley, 2010.
- [48] H. Bagci, A. E. Yilmaz, J.-M. Jin, and E. Michielssen, “Fast and rigorous analysis of EMC/EMI phenomena on electrically large and complex cable-loaded structures,” *IEEE Trans. Electromagn. Compat.*, vol. 49, pp. 361–381, May 2007.
- [49] E. Anderson, Z. Bai, C. Bischof, L. Blackford, J. Demmel, J. Dongarra, J. Du Croz, A. Greenbaum, S. Hammarling, A. McKenney, and D. Sorensen, *LAPACK Users’ Guide*. Warrendale, PA: SIAM, 1999.

- [50] S. Turley, “Acoustic scattering from a sphere,” *Class Notes, Department of Physics and Astronomy, Brigham Young University, Provo, UT*, 2006.
- [51] S. Yan, J.-M. Jin, and Z. Nie, “Accuracy improvement of the second-kind integral equations for generally shaped objects,” *IEEE Trans. Antennas Propag.*, vol. 61, pp. 788–797, Oct. 2012.
- [52] H. Bagci, F. P. Andriulli, K. Cools, F. Olyslager, and E. Michielssen, “A Calderón multiplicative preconditioner for the combined field integral equation,” *IEEE Trans. Antennas Propag.*, vol. 57, pp. 3387–3392, Oct. 2009.